Communications in Computational Chemistry
Commun. Comput. Chem. Vol. 8, No. 1, 83–96
doi: 10.4208/cicc.2025.282.01
Regular Article

Photoinduced Symmetry-Breaking Charge Separation Dynamics of Perylene Diimide Dimers: A Nonadiabatic Dynamics Simulation

Siyu Xiong[1], Meijie Jiang[1], Gaoyi Li[1] and Xiangyang Liu[1,*]

[1] *College of Chemistry and Material Science, Sichuan Normal University, Chengdu 610068, China.*

[*] Corresponding author: xiangyangliu@sicnu.edu.cn.

Received 9 Oct. 2025; Accepted (in revised version) 5 Jan. 2026

Abstract: In this work, we systematically investigate the photoinduced dynamics of two perylene diimide (PDI) dimers exhibiting symmetry breaking, namely PDI-CH_3 and PDI-iso, in both the gas phase and dichloromethane (DCM) with the combination of the optimally tuned screened range-separated hybrid (OT-SRSH) functional, the polarizable continuum model (PCM) and linear-response time-dependent density functional theory (LR-TDDFT) based nonadiabatic molecular dynamics (NAMD) simulations. The results demonstrate that both substituent effects and solvent effects influence the excited-state properties and dynamic processes of symmetry-broken PDI dimers significantly. In the gas phase, PDI-CH_3 exhibits negligible electron or hole transfer, whereas PDI-iso undergoes photoinduced energy transfer (PEnT). In DCM, the solvent effect not only reduces the excited-state energies of both structures but also alters their photoinduced dynamics by regulating the orders of different types of excitons. In short, PDI-CH_3 exhibits a photoinduced hole transfer (PHT)-dominated mechanism, while PDI-iso shifts from photoinduced energy transfer (PEnT) to concurrent hole transfer (PHT) and electron transfer (PET), facilitating the charge separation process. Moreover, this work indicates that introducing small substituents, i.e., methyl groups, at the bay positions of PDI to disrupt symmetry can also effectively modulate its photoinduced processes, providing a theoretical foundation for designing novel high-performance optoelectronic devices.

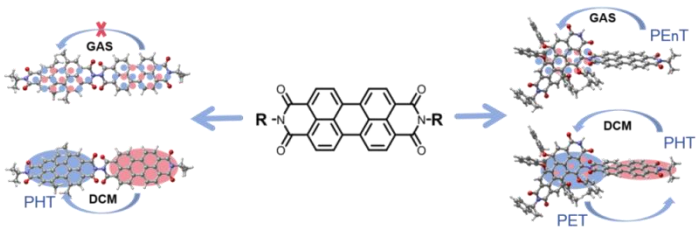

Key words: organic donor-acceptor, nonfullerene acceptor, symmetry breaking charge separation, PDI dimers, nonadiabatic dynamics simulation.

1. Introduction

The large-scale utilization of fossil fuels has led to increasingly prominent environmental issues such as atmospheric pollution and the greenhouse effect. Moreover, their non-renewable nature also continuously increases the risk of resource depletion. Consequently, the replacement of these fossil fuels with novel and renewable energy sources has become an inevitable trend [1-4]. Among various renewable energy sources, solar energy has emerged as a core alternative to traditional fossil fuels due to its ubiquitous distribution, ease of access, and virtually limitless supply [5-8]. Within the technologies for solar energy development and utilization, photovoltaic technology, which directly converts light into electricity via solar cells, has become a critical breakthrough in addressing the dual challenges of energy and environment, owing to its potential application scenarios [6,9-12].

The ability of organic solar cells to achieve photoelectric conversion fundamentally resides in their core donor-acceptor (D-A) heterojunction structure. This structure is composed of both an organic donor material and an acceptor material, and the performance compatibility between the two directly dictates the cell's charge separation efficiency and overall energy conversion performance [13-16]. Therefore, the development of donor or acceptor materials with superior properties is regarded as a fundamental strategy for enhancing the core performance of organic solar cells. In the evolution of organic solar cells, the selection of acceptor materials has undergone significant iterations and upgrades [17-19]. Fullerene-based acceptors, owing to their exceptional electron mobility, high electron affinity, and rapid photo-induced charge separation, once constituted the most widely utilized class of acceptor materials in organic solar cells [20]. However, constrained by inherent limitations such as low absorption coefficients in the visible region, difficulties in

diversifying molecular structures, and persistently high fabrication costs, fullerene-based acceptors have struggled to facilitate further breakthroughs in solar cell performance. These challenges have promoted the development of non-fullerene acceptors, which have achieved remarkable progress in recent years. Compared to traditional fullerene materials, they exhibit two distinct advantages: firstly, a broader absorption spectrum and a higher extinction coefficient, enabling more effective capture of solar photons; secondly, their unique electronic structure facilitates innovative charge separation pathways-not only electron transfer from donor to acceptor (Channel I mechanism) but also hole transfer from acceptor to donor (Channel II mechanism) [21-23]. The synergistic effect arising from this dual-channel charge generation mechanism significantly enhances charge generation efficiency, serving as a key driver for the improvement of power conversion efficiency (PCE) [24-26]. Currently, organic solar cells incorporating these materials have achieved PCEs exceeding 20%, thereby fully demonstrating their considerable potential for photovoltaic applications [27,28].

Perylene diimide (PDI) integrates a suite of advantages, including strong light absorption, high electron mobility, tunable energy levels, and excellent stability, making it one of the ideal materials for designing high-performance non-fullerene acceptors (NFAs) [29-32] (see **Figure S1** for the skeletal formula of PDI). For instance, Lin et al. reported a novel, nonplanar, star-shaped PDI acceptor using triphenylamine (TPA) as core to achieve a record high PCE for solution-processed OSCs based on non-fullerene acceptors at that time [33]. Later on, Zhong et al. designed helical PDI acceptors and further improved the PCE to ca. 6%. With the aid of femtosecond transient absorption spectroscopy, they proposed that the charge carriers are created from photogenerated excitons in both the electron donor and acceptor phases [34]. Meng et al. subsequently reported a bay-linked PDI dimer, in which selenium atoms were incorporated into the perylene core [35]. The introduction of selenium atom to the PBI core results in a high lowest unoccupied molecular orbital (LUMO) level, a twisted molecular configuration, and a high electron mobility, which are all beneficial for the photoinduced charge transfer process. After these pioneering works, a plenty of works have been conducted to explore the the relationship between molecular geometric structures of the PDI-based acceptors and OSCs performance [36-43]. Up till now, it is well established that PDI-based NFAs exhibiting twisted dimer, quasi-three-dimensional (3D), and 3D architectures usually show superior performance relative to those of the planar analogues.

Despite these achievements, the relationship between charge separation/charge recombination dynamics and the molecular geometry is complicated and still uncertain at ultrafast time scales, which motivate many time-resolved spectroscopic studies. For example, Kong et al. explored the intramolecular excited-state symmetry breaking charge separation (SB-CS) and charge recombination (CR) dynamics of two symmetric phenyl-methane-based PDI derivatives, a twist dimer PM-PDI2 (phenyl-methane-based PDI dimer) and a 3D configuration tetramer PM-PDI4 (phenyl-methane-based PDI tetramer), in different solvents with ultrafast femtosecond transient absorption spectroscopy and quantum chemical calculations. Based on the results, they concluded that the kinetics of CS and CR processes are strongly related to the molecular geometric structure, and the excited-state symmetry breaking in the 3D structure acceptor has superior photogenerated charge and photovoltaic properties [44]. Alzola et al. use transient absorption and emission spectroscopies to investigate the competition between SB-CS, fluorescence, and internal conversion in three related PDI dimers linked at the head land positions with o-, m-, and p-phenylene moieties, namely *o*-PDI2, *m*-PDI2, and *p*-PDI2 respectively. It is found that o-PDI2 exhibits SB-CS while m-PDI2 and p-PDI2 exhibit accelerated internal conversion due to the motion of the linker along with subnanosecond intersystem crossing (ISC) [45]. Very recently, Mazumder demonstrated the triplet excited-state population in a conformationally rigid perylenediimide trimer (PDI-T) via intramolecular symmetry-breaking charge separation (SB-CS) at the single-molecule level and the solvent effects are found to be important for the triplet quantum yield [46].

Apart from these experimental works, theoretical studies have also been performed to elucidate the underlying excited state mechanism for PDI based systems. However, most of them are concentrated on the static electronic structure calculations while the ultrafast dynamics remain unclear [37,38,47,48]. Until recently, nonadiabatic dynamics simulations are conducted by some groups to elucidate the photodynamics of PDI based donor-acceptor systems. For instance, Polkehn established that molecular packing determines charge separation in a liquid crystalline bisthiophene-PDI donor-acceptor material with quantum dynamical calculations using the Multi-Layer Multi-Configuration Time-Dependent Hartree (ML-MCTDH) method [49]. Recently, our group has also employed mixed-quantum-classical nonadiabatic dynamics to investigate the photoinduced dynamics of PDI based systems including the excitation wavelength-dependent charge generation dynamics in a PTB7/PDI donor-acceptor interface [50], the solvent dependent charge transfer in zinc phthalocyanine-PDI dyads [51], and the exciton dynamics in a PDI π-stack [52].

In most researches on non-fullerene acceptor materials, the construction of PDI dimers primarily relies on covalent bridging at the bay and head land position, whereas dimeric systems formed by direct N-N linkage between imide nitrogen atoms remain scarcely explored. In 2019, Fang and colleagues synthesized a series of head-to-tail PDI dimers (e.g., 1-1, 2-2). These dimers connect identical or different PDI units via N-N covalent bonds. They first conducted steady-state absorption and emission spectroscopy experiments, and the results showed that the fluorescence quantum yield of the twisted tetra-phenoxyl-substituted PDI dimer with symmetry-broken structure was significantly lower than that of the symmetric structure (0.89 vs. <0.01), suggesting that this structure might undergo ultrafast charge transfer processes leading to fluorescence quenching. Subsequent femtosecond time-resolved transient absorption spectroscopy experiments further validated this, revealing two ultrafast processes in the symmetry-broken structure with time scales of 300 fs and 14 ps. These two ultrafast processes were assigned as ultrafast energy transfer and charge separation, respectively. In contrast, no such processes were observed in the symmetric structure, where the system mainly deactivates to the ground state through fluorescence emission [53].

These results demonstrate that the introduction of substituents at the bay position, which breaks the symmetry of the PDI dimer, is the key factor enabling charge separation. Therefore, the rational design of dimer structures with tailored symmetry breaking provides a viable pathway to control the charge separation process, which plays a critical role in modulating the optoelectronic properties of the system.

To further elucidate the mechanism underlying these

phenomena, our group has recently conducted a systematic theoretical investigation into the excited-state dynamics of representative dimers synthesized by Fang et al., employing a combined approach of excited-state electronic structure calculations and nonadiabatic dynamics simulations. Our findings collectively demonstrate that both symmetry breaking and solvent effects significantly govern the excited-state dynamics of PDI dimers linked via imide nitrogen atoms. This insight provides a theoretical foundation for designing and optimizing novel symmetry-broken PDI dimers to enhance the performance of optoelectronic devices [54].

While previous research has yielded significant insights, a number of questions remain unanswered. Two immediate questions arise. First, both the experiments and prior theoretical studies employed bulky phenoxyl groups as bay-position substituents, which inevitably induced significant structural distortions. Would the same effects be observed if smaller methyl groups were used instead? Second, while retaining the phenoxyl substituents, would altering the connectivity between the two PDI monomers—for instance, linking them via the N and ortho positions—yield fundamentally different outcomes. To this end, we designed two distinct structures. The first retains the architecture of dimer 1-1 from the experimental study but replaces the phenoxyl substituents with methyl groups, leaving all other features unchanged. The second retains the phenoxyl substituents but alters the connectivity by linking the monomers between the N and ortho positions. These two structures are designated as PDI-CH_3 and PDI-iso, as shown in **Figure 1**. Based on these two model systems, we investigated the excited-state dynamics of these structures using LR-TDDFT, combined with static electronic structure calculations and nonadiabatic dynamics simulations. The results reveal that both substituent and solvent effects continue to exert a critical influence on the symmetry-breaking charge separation (SBCS) process in this class of systems [55]. This work provides a theoretical foundation for the subsequent design of novel PDI-based optoelectronic devices.

2. Simulation details

The minimum energy structures of PDI-CH_3 and PDI-iso were first optimized using the Perdew-Burke-Ernzerhof (PBE) functional with D3 dispersion correction proposed by Grimme et al, and all atoms were described using the 6-31G* basis set [56-60]. Given that both systems involve charge-transfer excited states, we decided to compute their excited-state properties using a range-separated hybrid (RSH) functional LC-PBE0. Moreover, to enhance the accuracy and take into account the solvent effects properly, the optimally tuned range-separation parameter approach in combination with the screened RSH technique, i.e., the OT-SRSH functional, were adopted. In this method, two key parameters of the original RSH functional, i.e., the range-separation parameter ω and the long-range correction parameter β, were optimized before LR-TDDFT calculations [61]. Specifically, the ω parameter was optimized according to the IP theorem, yielding range-separation parameters of 0.1216 and 0.0942 for PDI-CH_3 and PDI-iso dimers in the gas phase, respectively. Subsequently, based on the optimized ω parameter and in combination with the polarizable continuum model (PCM) using dichloromethane (DCM) as the solvent, the long-range correction parameter β in DCM was further optimized, yielding values of -0.1191 and -0.1328, respectively. Using the optimized ω and β parameters in conjunction with the PCM solvent model, LR-TDDFT calculations were performed to investigate the excited states of the systems in solution. In short, we set the α parameters to the default value, i.e., 0.25, of LC-PBE0 functional in this work. In gas phase, the β parameters are set to 0.75 so that the long range limit of the exact exchange, i.e., the sum of α and β, equals 1.0; for solvated systems, the long range limit of the exact exchange should be close to 1/ε, where ε represents the dielectric constant of the solvent. Therefore, β values should be close to -0.1380 for both molecular structures in dichloromethane with a dielectric constant of 8.93, which are close to our optimized values of -0.1191 and -0.1328 for PDI-CH_3 and PDI-iso. The sum of α and β is 0.1309 and 0.1172 for PDI-CH_3 and PDI-iso respectively in dichloromethane. The optimized ω parameters are used for both gas and solvent calculations. To distinguish it from the original LC-PBE0 functional, the parameter-optimized version is denoted as LC-PBE0*, which has demonstrated excellent applicability in previous studies [55,61-64].

The NAMD simulations were then conducted using the fewest-switches surface hopping algorithm based on classical path approximation (FSSH-CPA) method at the LR-TDDFT level implemented in the GTSH program to examine the excited-state dynamics of the PDI-CH_3 and PDI-iso dimers [65,66]. All excited-state calculations required during NAMD simulations were performed using the OT-SRSH functional LC-PBE0*. Moreover, the numerical calculation of the time derivative non-adiabatic couplings (TDNACs) between the electronic states of both structures was performed using an orbital based algorithm [66-69]. In the FSSH-CPA dynamics, empirical quantum decoherence correction proposed by Granucci et al. was implemented with a correction value set to 0.1 a.u. [70-72]. Moreover, the NAMD simulations were conducted based on the classical path approximation (CPA), which has been demonstrated to accurately describe excited-state relaxation processes without involving significant conformational changes, bond formation, or bond cleavage [66-68,73-75]. The minimum energy structures of PDI-CH_3 and PDI-iso were initially heated to 300 K and equilibrated for approximately 1 ps using a Nosé-Hoover chain thermostat with a chain length of 5 [57,60,76,77]. Subsequently, 3 ps NVE molecular dynamics simulations were performed, generating 1000 initial conditions stochastically based on vertical excitation energies and oscillator strengths. All ab initio adiabatic molecular dynamics (AIMD) simulations were performed using the PBE+D3 method with a time step of 1 fs. The obtained 3 ps NVE ground-state trajectory was utilized for subsequent FSSH-CPA simulations. Starting from each initial condition, 300 FSSH-CPA trajectories were propagated with a time step of 1 fs. The final statistical results were obtained by averaging over the 1000×300 trajectories. It should be noted that under the classical path approximation, the simulation requires only a ground-state trajectory and all relevant energies and TDNACs between different states required for the FSSH algorithm only need to be calculated once. Using this predefined ground-state trajectory, various initial conditions, i.e., starting points for the surface hopping trajectories, can be selected for propagation. Since there is no need to compute energies, gradients, or TDNACs on-the-fly under this approximation, the surface hopping algorithm can be executed with high efficiency. As a rough approximation, the classical path approximation may influence the timescales of photodynamics. However, the exact effects remain unclear, as direct comparisons are challenging due to

the prohibitively high computational cost of performing on-the-fly nonadiabatic molecular dynamics (NAMD) simulations for large systems. Nevertheless, NAMD simulations employing the CPA have been shown to yield qualitatively—and in some cases, quantitatively—accurate timescales when compared to experimental observations, as demonstrated in several studies by our group and others [67,68,73,78-81]. Therefore, we believe that despite the rough approximation, the CPA approximation can still provide valuable insights into the photophysics of large and rigid organic donor-acceptor systems. In order to reflect detailed balance condition under classical path approximation, hop rejection and velocity rescaling were replaced by scaling transition probabilities $p_{kj}(t)$ with a Boltzmann factor

$$p_{kj}(t) = p_{kj}(t)b_{kj}(t)\ (E_j > E_k). \quad (1)$$

where, $b_{kj} = \exp\left(-\frac{E_j - E_k}{k_B T}\right)$. This strategy has been successfully applied to nonadiabatic dynamics simulations of various materials [66,67,73,74,77]. All geometry optimizations and LR-TDDFT calculations were carried out using GAUSSIAN 09 [82]. The optimized ω and β parameters were obtained using the optDFTω program, which was originally developed by Lu et al. and subsequently modified locally [83]. AIMD simulations were conducted using the QUICKSTEP module in CP2K23.1, employing the DZVP-MOLOPT-SR-GTH basis set and Goedecker-Teter-Hutter (GTH) pseudopotentials at the PBE+D3 level of theory [84-89]. All nonadiabatic dynamics simulations were performed using the GTSH software package [65]. The relevant electron and hole densities were computed using Multiwfn 3.8 [90,91]. Additional theoretical background can be found in our previous works.

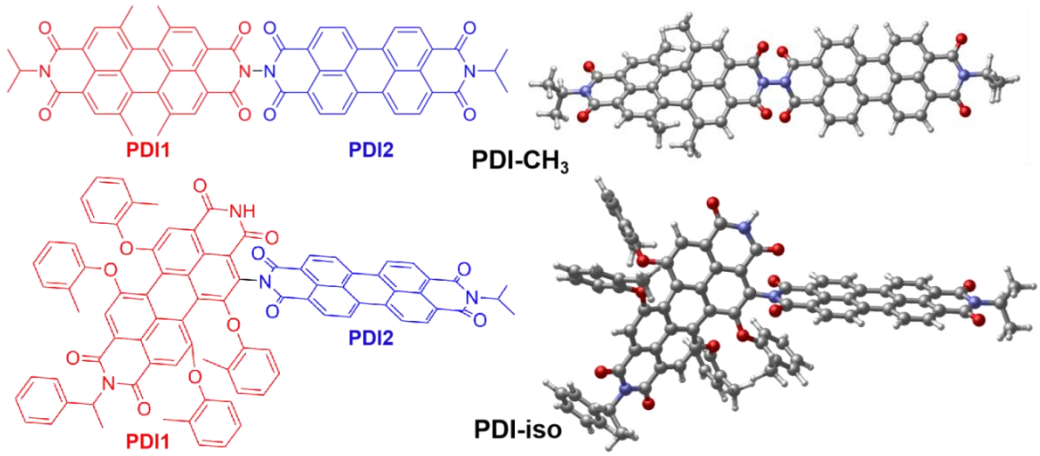

Figure 1. The chemical structures of PDI-CH_3 and PDI-iso and their corresponding three-dimensional structures optimized at the PBE + D3 level.

3. Results and discussion

We first employed the PBE+D3 method to optimize the ground-state minimum-energy structures of PDI dimers linked by covalent bonds with different monomers, labeled PDI-CH_3 and PDI-iso, as shown in **Figure 1**. As can be seen, significant spatial hindrance from the carbonyl groups causes non-coplanar orientations between the PDI1 and PDI2 fragments in the stable configurations of both dimers. Moreover, the introduction of the methyl groups and phenoxyl groups into the PDI1 units of the two structures results in distinct effects: the methyl groups induce a moderate distortion within the PDI1 fragment, while the phenoxyl groups lead to a more pronounced distortion. In contrast, the three-dimensional structure of PDI2 deviates only minimally from the skeletal formula representation (**Figure S1**), except for the terminal side-chain groups, with the PDI2 fragments in both configurations maintaining a planar geometry. The conformational distortion induced by the introduction of functional groups disrupts the original structural symmetry, potentially leading to substantial modifications in the system's electronic structure and ultimately influencing its photoinduced excited-state dynamics. Additionally, the different substituents and connection patterns in PDI-CH_3 and PDI-iso may also lead to different excited state properties, as illustrated in the following sections. We have also optimized these structures without dispersion correction. As shown in **Figure S2**, the overlap between the structures optimized with and without dispersion correction are very close to each other, indicating that the van der Waals interaction may have small influence on the dimer structures.

Based on the optimized structures and using the optimally tuned LC-PBE0* functional, we performed LR-TDDFT calculations to determine the lowest ten singlet excited states for both PDI-CH_3 and PDI-iso dimers in the gas phase and DCM. These excited states are crucial for understanding the photoinduced dynamics of donor-acceptor systems. Additionally, the distributions of electron and hole densities for these excited states were analyzed using the Multiwfn 3.8 software. The spatial distributions of electron and hole densities, along with the corresponding vertical excitation energies, are shown in **Figure 2** and **Figure 3**. In these figures, blue and red colors represent the distribution of electron and hole and electron densities, respectively.

We begin by discussing the excited-state properties of PDI-CH_3 (**Figure 2**) in both the gas phase and DCM. Based on the electron and hole density distributions, the ten electronic excited states in the gas phase can be categorized into four distinct types. The most prevalent category consists of local excitation (LE) states on PDI1 (PDI1→PDI1), where both the electron and hole are localized on the PDI1 fragment. This category includes the S_4 (3.50 eV), S_6 (3.58 eV), S_7 (3.61 eV), and S_{10} (3.78 eV) states. Similarly, we also identified LE states on PDI2, which include S_3 (3.44 eV), S_8 (3.66 eV), and S_9 (3.69 eV). The third category consists of the S_1

(2.54 eV) and S_2 (2.68 eV) states, where the electron and hole are no longer localized on a single fragment but are delocalized across both PDI1 and PDI2. These states likely represent hybrid states composed of a mixture of LE and charge transfer (CT) states character. In the S_1 state, the LE character of PDI2 dominates, while in the S_2 state, the LE character of PDI1 dominates. The fourth category is represented by the S_5 (3.51 eV) state, in which the hole is primarily localized on PDI1, while the electron is distributed on PDI2, indicating a CT state from PDI1 to PDI2. Since the bright LE states are lowest in gas for PDI-CH_3, it is expected that strong fluorescence might exist, as observed in previous experimental work [53]. Therefore, we additionally simulated the absorption and emission spectrum of PDI-CH_3 in gas phase using the minimum-energy structures in ground and excited states only. As shown in **Figure S5**, apart from the red shift of emission spectrum, the strength of the emission is only slightly weaker than absorption, implying the strong fluorescence of this structure in gas phase. It is safely to postulate that similar phenomena can be observed for other structures with lowest LE states. Since the calculation of emission spectrum require the optimization of the lowest excited states, considering the large size of another structure, we will not discuss relevant emission spectra subsequently.

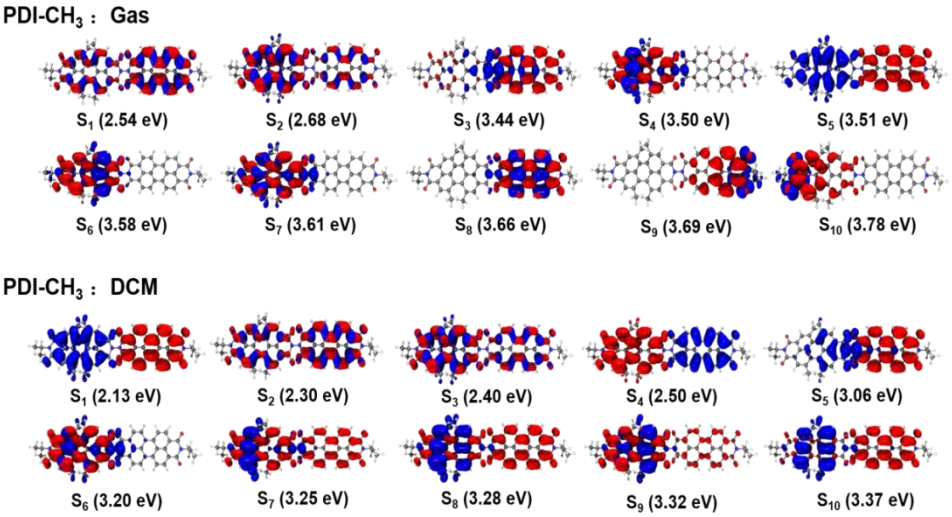

Figure 2. The electron (red) and hole (blue) densities of the fifteen lowest singlet excited states of photoinduced PDI-CH_3 at the Franck-Condon point in the gas phase and DCM calculated using TD-LC-PBE0*. Also shown are the corresponding vertical excitation energies.

Compared to the excited states in the gas phase, those in DCM show changes in both the nature of the excited states and their vertical excitation energies due to solvent effects. First, in addition to the three types of excited states present in the gas phase, a pure CT state from PDI2 to PDI1 (PDI2→PDI1) emerges, identified as the S_4 state. Secondly, there are states where the hole is localized on PDI1, while the electron is delocalized across both PDI1 and PDI2, specifically the S_7, S_8, S_9, and S_{10} states. Finally, the excitation energies of all ten states show an overall decrease. According to these facts, we propose that even though the methyl group (-CH_3) is a weak electron-donating substituent that causes only a slight perturbation to the electronic structure of the PDI conjugated system, it may also introduce significant solvent dependent SBCS dynamics in DCM. This hypothesis is supported by subsequent NAMD simulations.

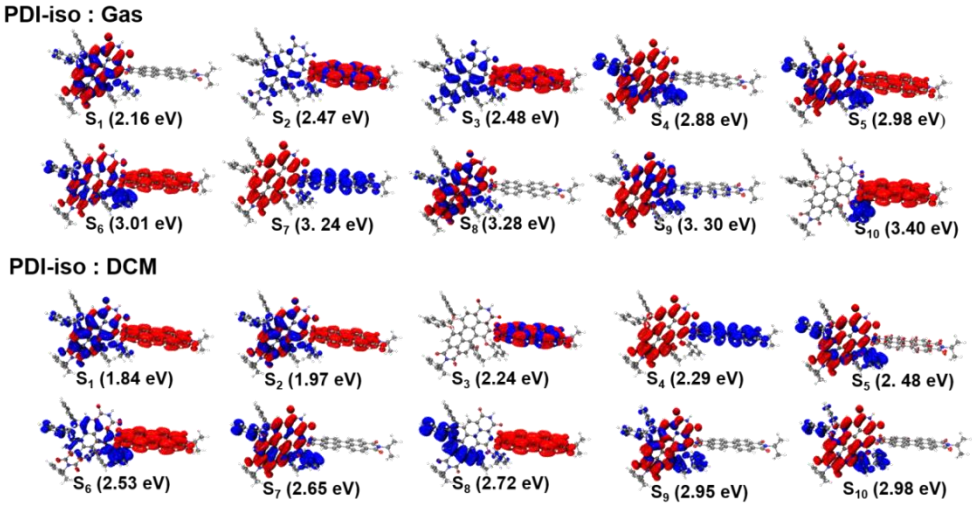

Figure 3. The electron (red) and hole (blue) densities of the fifteen lowest singlet excited states of photoinduced PDI-iso at the Franck−Condon point in the gas phase and DCM calculated using TD-LC-PBE0*. Also shown are the corresponding vertical excitation energies.

We apply the same methodology to analyze the excited-state properties of PDI-iso (**Figure 3**). In the gas phase, these states can be roughly categorized into five types. The first and most predominant category consists of states where both the electron and hole are localized on PDI1, including S_1, S_4, S_8, and S_9. These are classified as LE states on PDI1. The second category includes the S_2 and S_3 states, where the electron and hole are primarily localized on PDI2 but a minor portion of the hole also residing on PDI1, representing the dominant LE state of PDI2. The third category, which includes S_5 and S_6 states, represents hybrid states arising from a mixture of LE and CT character. The fourth category is the S_7 state, where the electron is localized on PDI1 and the hole on PDI2. This distribution can be regarded as a CT state from PDI2 to PDI1 (PDI2→PDI1). The fifth and final category is the S_{10} state, characterized by a small portion of the hole concentrated on one side chain of PDI1 and a large portion of the electron localized on PDI2, which can be considered a special CT state from PDI1 to PDI2.

In the DCM solvent, several changes occur in the nature of the excited states and their vertical excitation energies. For example, all state energies are much lower than those in gas phase. Additionally, the lowest lying state changes from being an LE state on PDI1 to a CT state from PDI1 to PDI2. These results suggest that solvent effects will also influence the photodynamics of PDI-iso upon excitation.

Based on the vertical excitation energies of the excited states, we employed the semiclassical method proposed by Barbatti et al. to simulate the UV-Vis absorption spectra of the PDI-CH_3 and PDI-iso dimers in both the gas phase and DCM solvent [92,93]. This calculation utilized 1000 structures obtained from ground-state molecular dynamics simulations. A key advantage of this approach is its ability to account for the influence of nuclear thermal motion on the absorption spectra. The resulting absorption spectra are presented in **Figure 4**. Furthermore, based on the fragment-based exciton analysis of excited-state properties, we can determine the contributions of different types of excitons generated at specific excitation wavelengths. The two types of LE excitons produced upon excitation are denoted as |PDI1*⟩and |PDI2*⟩, while the two CT excitons are denoted as |PDI1$^+$PDI2$^-$⟩and |PDI1$^-$PDI2$^+$⟩. The decomposed spectra of two structures in both the gas phase and DCM are shown in **Figures 4(a)**, **4(b)**, **4(c)**, and **4(d)**.

In the gas phase, the absorption spectrum of PDI-CH_3 (**Figure 4(a)**) is characterized by a broad band with its maximum at 496 nm. Excitation around 496 nm generates four types of excitons. Among these, the LE excitons |PDI2*⟩ and |PDI1*⟩ contribute most significantly, followed by the CT excitons |PDI2$^-$PDI1$^+$⟩ and |PDI2$^+$PDI1$^-$⟩. In contrast, the absorption spectrum of PDI-iso (**Figure 4(b)**) exhibits two distinct bands with maxima at 512 nm and 554 nm, respectively. The absorption at 512 nm is predominantly composed of the LE exciton |PDI2*⟩, followed by the CT exciton |PDI1$^+$PDI2$^-$⟩. Conversely, the absorption at 554 nm is primarily due to the LE exciton |PDI1*⟩. These results suggest that the methyl groups have less influence on the LE states of the PDI fragments compared to the phenoxyl groups.

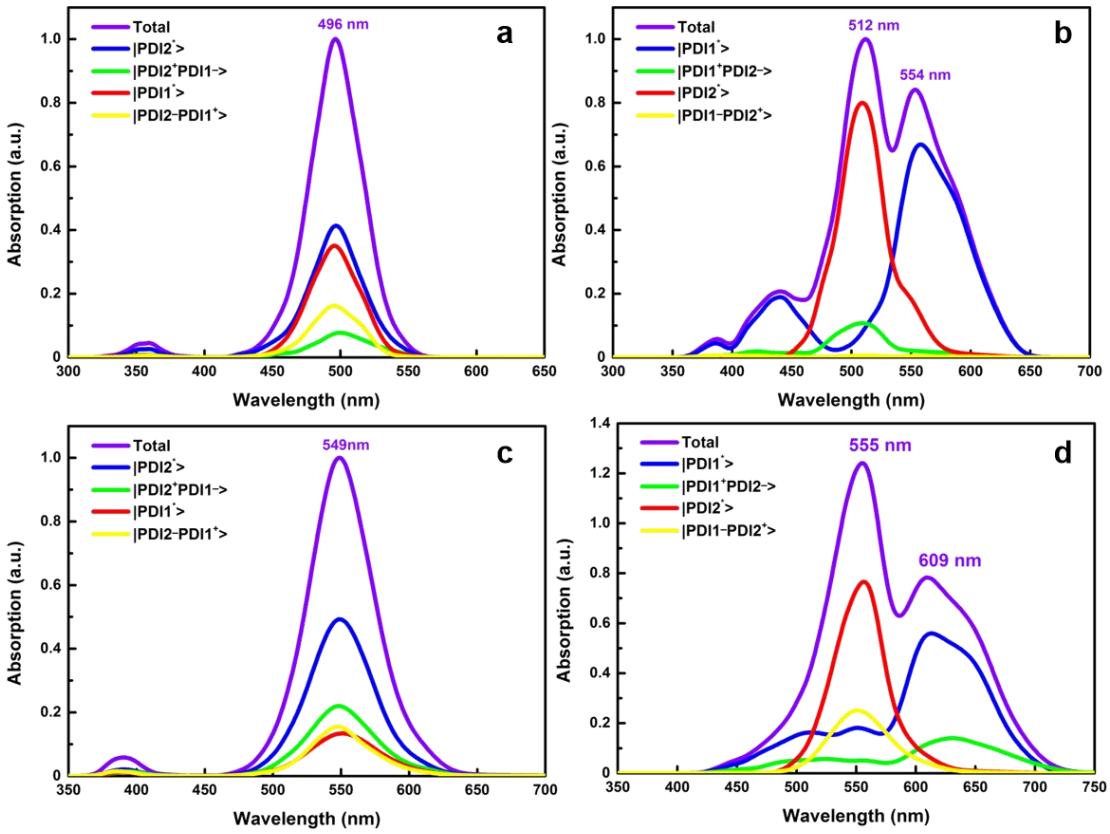

Figure 4. Simulated absorption spectra of PDI-CH_3 (a) and PDI-iso (b) in the gas phase and PDI-CH_3 (c) and PDI-iso (d) in DCM, calculated using the OT-SRSH functional LC-PBE0* with 1000 snapshots obtained from the ground-state MD trajectory with the weights of different excitons also shown.

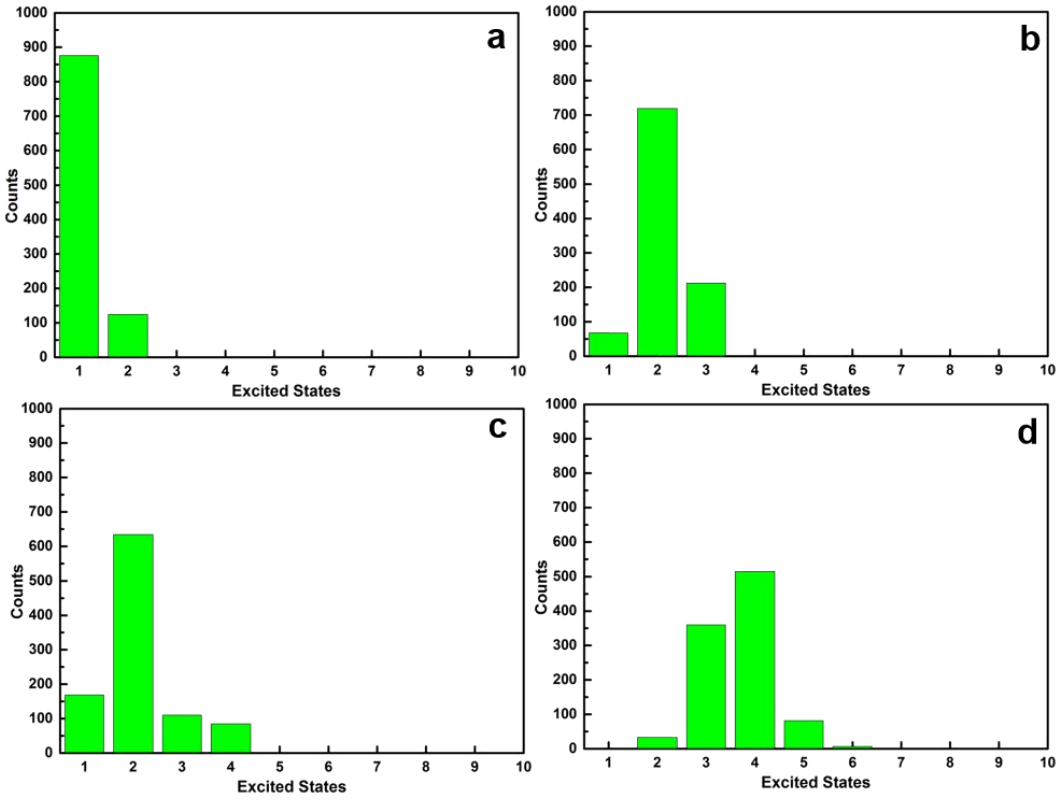

Figure 5. The distributions of selected initial excited states in FSSH-CPA simulations for PDI-CH_3 (a) and PDI-iso (b) in the gas phase and PDI-CH_3 (c) and PDI-iso (d) in DCM.

When solvent effects are considered, both dimers exhibit significant red-shifting the absorption peaks. In **Figure 4(c)**, the absorption peak of PDI-CH_3 shifts from 496 nm in gas phase to 549 nm in solution. At 549 nm, the absorption is mainly composed of the LE exciton |PDI2*⟩, followed by |$PDI2^+PDI1^-$⟩. Unlike in the gas phase, the contribution from the LE exciton |PDI1*⟩ is significantly reduced. For PDI-iso (**Figure 4(d)**), the peak at 512 nm shifts to 555 nm, and the peak at 554 nm shifts to 609 nm. Upon excitation near 555 nm, the absorption is predominantly composed of the LE exciton |PDI2*⟩. A key difference from the gas phase is the emergence of the CT exciton |$PDI1^-PDI2^+$⟩, which changes from being nearly absent to becoming the second-largest contributor. Simultaneously, the contribution from the LE exciton |PDI1*⟩ also increases. For excitation at 609 nm, the absorption is primarily composed of the LE exciton |PDI1*⟩, while the CT exciton |$PDI1^+PDI2^-$⟩ appears as the second largest contributor.

In our previous work, we have also calculated the spin orbit couplings (SOCs) between relevant singlet and triplet states [54]. It turns out that all these SOCs are very small and the largest value is no more than 5 cm^{-1}, indicating that the intersystem crossing should be much slower and cannot compete with the ultrafast dynamics completed in a few picoseconds. As an extension of our previous work, since we only changed the connection pattern or induced methyl substituents in this study, the SOCs are expected to be very small as before. Consequently, the triplet states would be less important in the ultrafast dynamics and are not considered in this work.

While the static electronic structure calculations of the excited states have provided substantial insights into the properties of these two dimers, the associated photoinduced dynamics remain unclear and require further investigation through NAMD simulations. Therefore, we performed NAMD simulations using the FSSH-CPA at the LR-TDDFT level to explore the photoinduced processes upon excitation at specific wavelengths for both PDI-CH_3 and PDI-iso in the gas phase and in DCM.

We began by selecting the initial excited states for FSSH-CPA simulations based on their vertical excitation energies and oscillator strengths. For instance, in the gas phase, the absorption peak of PDI-CH_3 at 496 nm (2.50 eV) corresponds to LE states localized on both the PDI1 and PDI2 fragments. The initial state selection followed two criteria: (1) the vertical excitation energy must fall within the range of 2.50 ± 0.3 eV, and (2) the oscillator strength of the state must be greater than a random number between 0 and 1. Based on these criteria, the resulting initial electronic state population for PDI-CH_3 upon excitation around 496 nm in the gas phase is shown in **Figure 5(a)**.

Using the same criteria, we also selected the initial states for excitation at 512 nm for PDI-iso in the gas phase (**Figure 5(b)**), at 549 nm for PDI-CH_3 in DCM (**Figure 5(c)**), and at 555 nm for PDI-iso in DCM (**Figure 5(d)**). As can be seen, in the gas phase, excitation around 496 nm of PDI-CH_3 (**Figure 5(a)**) leads to the excited state population primarily residing in S_1, with a minor contribution from the S_2 state. For PDI-iso (**Figure 5(b)**), the population after excitation is distributed across the S_1 to S_3 states, with the largest contribution from the S_2 state. In the DCM solvent, excitation around 549 nm of PDI-CH_3 (**Figure 5(c)**) results in the electronic state population being spread across S_1 to S_4, with the S_2 state contributing the most. For PDI-iso (**Figure 5(d)**), excitation at 555 nm results in the S_4 state dominating the population, followed by the S_3 state.

Based on the 1000 initial conditions selected above, we propagated 300 FSSH-CPA trajectories for each chosen initial

condition. The total simulation time was 500 fs for PDI-CH_3 in the gas phase and 3 ps for all other cases (both dimers in the gas phase and in DCM), with a time step of 1 fs. The final results were obtained by averaging over all 1000 × 300 trajectories. The resulting time-dependent state populations for both structures in gas phase and DCM are shown in **Figure 6**. We begin by discussing the excited-state populations in the gas phase. For PDI-CH_3 (**Figure 6(a)**), the initial population consists primarily of the S_1 and S_2 states. The weight of S_1 increases from approximately 0.88 to nearly 1.00 within 300 fs, while that of S_2 state decreases from around 0.12 to zero over the same time period. For PDI-iso (**Figure 6(b)**), the initial population is dominated by the S_2 state with a weight of approximately 0.71, while the S_3 state contributes about 0.21. Within 2 ps, the population of S_2 decreases from around 0.72 to approximately 0.02, while that of S_3 decays to zero. Concurrently, the weight of S_1 increases from 0.08 to about 0.98. The time evolutions of the excited-state populations for both structures in DCM are shown in **Figure 6(c)** and **Figure 6(d)**. At the initial time, the population of PDI-CH_3 (**Figure 6(c)**) is consistent with **Figure 5(c)**, with the S_2 state being the dominant contributor at a proportion of 0.63, while the S_3 and S_4 states make minor contributions. As time goes by, the populations of the S_2, S_3, and S_4 states decrease, while that of S_1 increases to approximately 0.97. For PDI-iso (**Figure 6(d)**), the initial population is primarily composed of the S_3, S_4, and S_5 states, with a minor contribution from S_2. The S_4 state has the largest weight at approximately 0.52, followed by S_5 at about 0.08. The population of the S_3 state initially increases from 0.38 to around 0.57 before eventually decaying, along with S_4 and S_5, to nearly zero by 2 ps. Conversely, the population of S_2 rises from 0.02 to approximately 0.13, while that of S_1 increases from zero to about 0.82. After that, the populations of S_1 and S_2 fluctuate around these values.

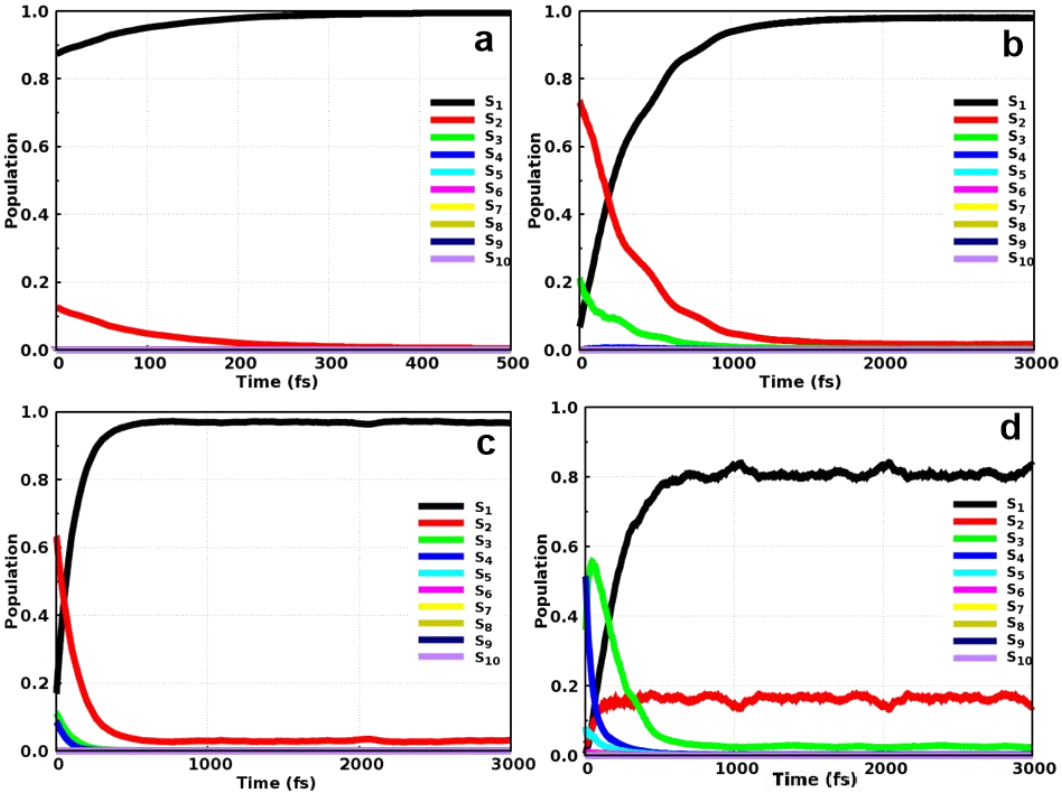

Figure 6. Time-dependent populations of relevant adiabatic excited states for PDI-CH_3 (a) and PDI-iso (b) in the gas phase and PDI-CH_3 (c) and PDI-iso (d) in DCM.

To further elucidate the mechanisms underlying the distinct relaxation processes observed in the two structures, we analyzed the average energy gaps between adjacent adiabatic states and the average absolute values of the TDNACs for both PDI-CH_3 and PDI-iso, as shown in **Figure 7**. It is well established that nonadiabatic transitions are governed by both the energy gap and the nonadiabatic coupling strength. The relationship between the nonadiabatic coupling vector and the energy gap is given by the following equation:

$$\mathbf{d}_{ij} = \frac{< \Psi_i \left| \frac{\partial \mathbf{H}}{\partial \mathbf{R}} \right| \Psi_j >}{E_j - E_i} \quad (1)$$

where $\mathbf{d}_{ij}$ is the nonadiabatic coupling vector between states i and j, and E_j and E_i are their respective energies. Since the TDNACs between adiabatic states i and j can be computed as $\Lambda_{ij} = \mathbf{v} \times \mathbf{d}_{ij}$, a smaller energy gap generally leads to a larger TDNAC and consequently a faster nonadiabatic transition rate.

As shown in **Figure 7(a)**, the energy gaps between adjacent states of PDI-CH_3 are predominantly distributed within 4.0 kcal/mol, with the most frequent values between 2.2 and 4.0 kcal/mol and an average value of 3.92 kcal/mol. Simultaneously, the TDNACs between adjacent states in the gas phase are mostly greater than 30 ps^{-1}, with an average value of 35.32 ps^{-1} for all adjacent electronic states. In **Figure 7(c)**, which corresponds to PDI-CH_3 in DCM, it can be observed that the average TDNACs for most adjacent states also exceed 30 ps^{-1}, with an overall average of 33.66 ps^{-1}. The energy gaps between adjacent states are primarily distributed between 1.0 and 4.0 kcal/mol, with a mean value of 2.82 kcal/mol.

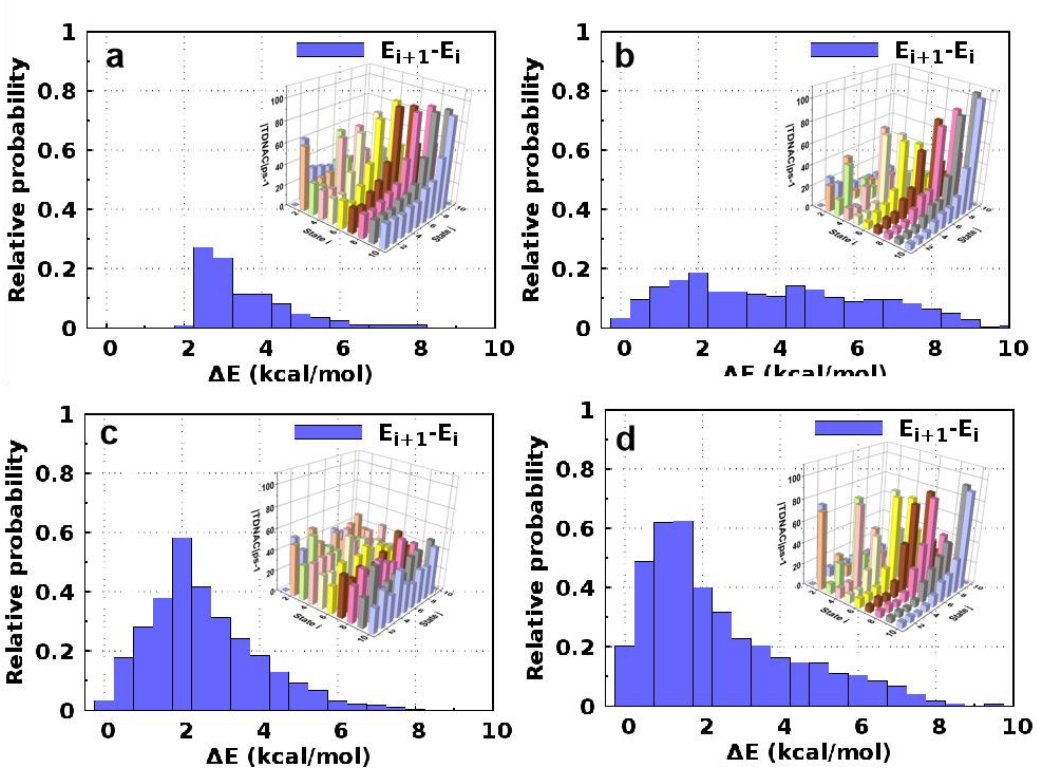

Figure 7. The distribution of energy gaps (E_{i+1}-E_i, in kcal/mol) between the ten lowest singlet excited-states and the averaged TDNACs (in ps^{-1}) between these electronic states for PDI-CH_3 (a) and PDI-iso (b) in the gas phase, as well as PDI-CH_3 (c) and PDI-iso (d) in DCM.

For PDI-iso (**Figure 7(b**) and **Figure 7(d)**), the average TDNACs between adjacent electronic states are 21.01 ps^{-1} in the gas phase and 22.53 ps^{-1} in DCM. The corresponding energy gaps between adjacent states are mainly distributed between 0 and 8 kcal/mol, with mean values of 4.31 kcal/mol (gas phase) and 2.69 kcal/mol (DCM), respectively. The small energy gaps and the large TDNACs accounts for the ultrafast photodynamics observed in these systems.

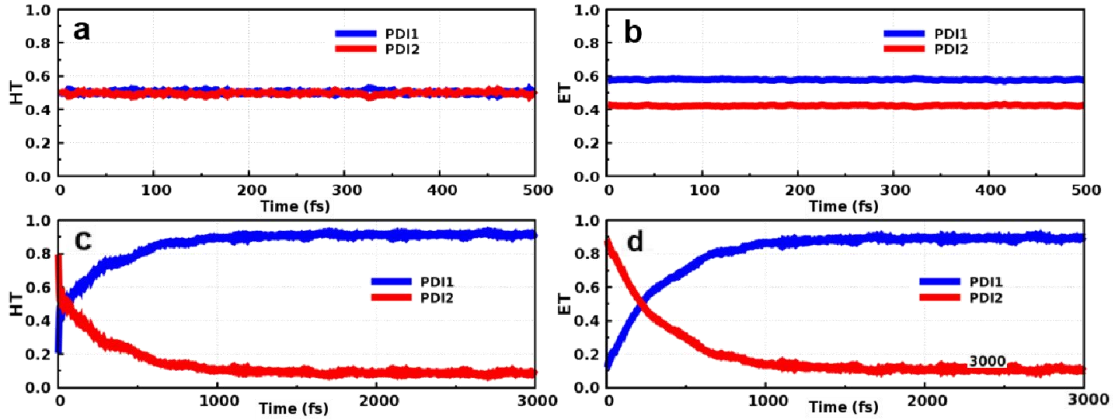

Figure 8. In the gas phase, the time-dependent weights of the holes (a) and electrons (b) for PDI-CH_3, and the weights of the holes (c) and electrons (d) for PDI-iso.

Based on the NAMD simulations, we can also derive the time-dependent electron and hole weights on different fragments of both dimers under two environments, as shown in **Figures 8-10**. We first discuss the gas-phase results. As shown in **Figure 8(a)** and **Figure (b)**, the electron and hole weights on both fragments of PDI-CH_3 remain nearly constant at around 0.5 throughout the 500 fs simulation, indicating that charge transfer is unlikely to occur with methyl substitution in the gas phase. Fragment-based exciton analysis (**Figure 10(a)**) reveals that the weights of various excitons remain essentially unchanged within 500 fs, further confirming this conclusion. In contrast, for PDI-iso (**Figure 8(c)** and **Figure 8(d)**), the initial hole and electron weights on the PDI2 fragment are significantly higher, with values of 0.80 and 0.88 respectively, indicating that the initial excitation primarily corresponds to a LE state on PDI2. Over time, the electron and hole weights on PDI2 gradually decrease, while those on PDI1 increase monotonically, suggesting the simultaneous occurrence of hole transfer (HT) and electron transfer (ET) from PDI2 to PDI1. Since both ET and HT occur in the same direction, this process corresponds to PEnT from PDI2 to PDI1. The time-dependent exciton weight evolution

(**Figure 10(c)**) further confirms this, showing that within 2 ps, the initial LE exciton |PDI2*⟩ and CT state |PDI1$^+$PDI2$^-$⟩ transform into the LE exciton |PDI1*⟩. Notably, the CT state |PDI1$^-$PDI2$^+$⟩ corresponding to electron transfer from PDI2 to PDI1 does not participate in the excited-state dynamics during the simulation.

We next examine the excited-state dynamics in DCM, as illustrated in **Figure 9**. For PDI-CH$_3$ (**Figure 9(a)** and **Figure (b)**), during the 3 ps simulation time, the hole weight on PDI1 increases monotonically from 0.50 to approximately 0.70 within 500 fs, while that on PDI2 decreases monotonically from 0.50 to around 0.30, indicating hole transfer from PDI2 to PDI1. Meanwhile, the electron weight shows only a minor transfer (~0.1) from PDI1 to PDI2, suggesting that the overall process is dominated by hole transfer, leading to the formation of the CT state |PDI1$^+$PDI2$^-$⟩ with a mixture of the LE exciton |PDI1*⟩. The time-dependent exciton weight variations (**Figure 10(b)**) confirms this picture, revealing that all four excitons in PDI-CH$_3$ participate in the excited state dynamics. For PDI-iso in DCM (**Figure 9(c)** and **Figure (d)**), the hole weight on PDI1 increases monotonically from approximately 0.20 to about 0.98 within 2 ps, while that on PDI2 decreases monotonically from 0.80 to around 0.02, indicating efficient hole transfer process from PDI2 to PDI1. Conversely, the electron weight on PDI1 decreases from 0.60 to approximately 0.30, while that on PDI2 increases from 0.40 to around 0.70, indicating electron transfer from PDI1 to PDI2. Since the electron and hole transfer in opposite directions, this process reflects a highly efficient charge transfer from PDI2 to PDI1 occuring within 1 ps. Fragment-based exciton analysis (**Figure 10(d)**) demonstrates that within 1 ps, the initial LE exciton |PDI2*⟩ and CT exciton |PDI1$^-$PDI2$^+$⟩ undergo conversion to the LE exciton |PDI1*⟩ and CT exciton |PDI1$^+$PDI2$^-$⟩. These results demonstrate that the dual inductive and steric effects of the isomeric substituents simultaneously influence electron distribution and modulate charge-transfer pathways through conformational torsion, resulting in markedly different excited-state dynamics for PDI-iso compared to PDI-CH$_3$.

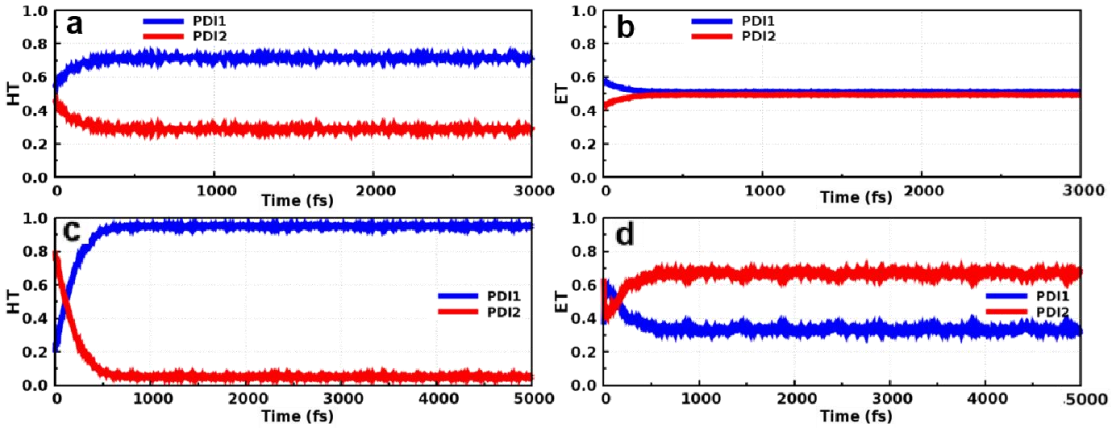

Figure 9. In DCM, the time-dependent weights of holes (a) and electrons (b) for PDI-CH$_3$ and the weights of holes (c) and electrons (d) for PDI-iso.

For the low-energy absorption peaks of PDI-iso in the gas phase (554 nm) and in dichloromethane (DCM, 609 nm), we performed nonadiabatic dynamics simulations using the same methodology as applied to the high-energy peaks. As shown in **Figure S3(a, b)**, after excitation in the gas phase, the electronic state population is primarily localized in the S_1 state (the LE state of PDI1), whereas in DCM, the S_2 state (where the hole is concentrated on PDI1 and the electron is distributed between PDI1 and PDI2, predominantly representing a CT state from PDI1 to PDI2) contributes the most, followed by the S_1 state. Further analysis of the time-dependent population changes of the relevant adiabatic states (**Figure S3(c, d)**) reveals that within the 3000 fs simulation time, no significant variations are observed in the population weights of the ten adiabatic states in the gas phase except for S_1 and S_2. In contrast, in DCM, the S_2 state initially contributes the largest population, followed by S_1, with population transfer from S_2 to S_1 occurring around 1000 fs. This observation is consistent with the initial excited-state population distribution. Based on the nonadiabatic dynamical simulations, **Figure S4** shows the time-dependent electron and hole weights of the low-energy peak of PDI-iso on different fragments in both environments. In the gas phase (**Figure S4(a, b)**), the electron and hole weights on the two fragments show no significant changes. However, in DCM (**Figure S4(c, d)**), due to the influence of solvent effects, a small amount of hole transfer from PDI2 to PDI1 and electron transfer from PDI1 to PDI2 are observed.

Finally, we would like to compare the results with our previous work to address the two questions raised at the beginning of this study. First, we confirmed that even a small methyl group can induce ultrafast charge transfer dynamics in polar solvents, suggesting that even minor perturbations in symmetric structures can lead to significant photoinduced dynamics in PDI dimers. Additionally, the solvent effect plays a crucial role in regulating the symmetry-breaking charge transfer dynamics. Second, although there are some small differences between PDI-iso and its N-N bridge isomer, the overall excited state properties and associated dynamics are very similar. This implies that modifying the monomer structure may be a more efficient way to regulate the photodynamics of PDI dimers than altering their connection patterns.

4. Conclusion

In summary, we investigated the photoinduced dynamics of PDI-CH$_3$ and PDI-iso in the gas phase and DCM environments with LR-TDDFT based static excited state electronic structure calculations and NAMD simulations. Our simulation results reveal

that both substitution and solvent effects have significant influences on the excited-state dynamics of PDI dimers. In the gas phase, PDI-CH_3 exhibits negligible electron or hole transfer, whereas PDI-iso undergoes photoinduced energy transfer from PDI2 to PDI1. In contrast, PDI-CH_3 changes from showing no transfer in the gas phase to being dominated by photoinduced HT (PDI2→PDI1) in DCM, while PDI-iso changes from photoinduced ET in the gas phase to simultaneous photoinduced HT (PDI2→PDI1) and ET (PDI1→PDI2) in DCM. These facts pave the way for the design of novel PDI exhibiting symmetry breaking charge separation properties, which can be helpful for enhancing the PCE of organic solar cells.

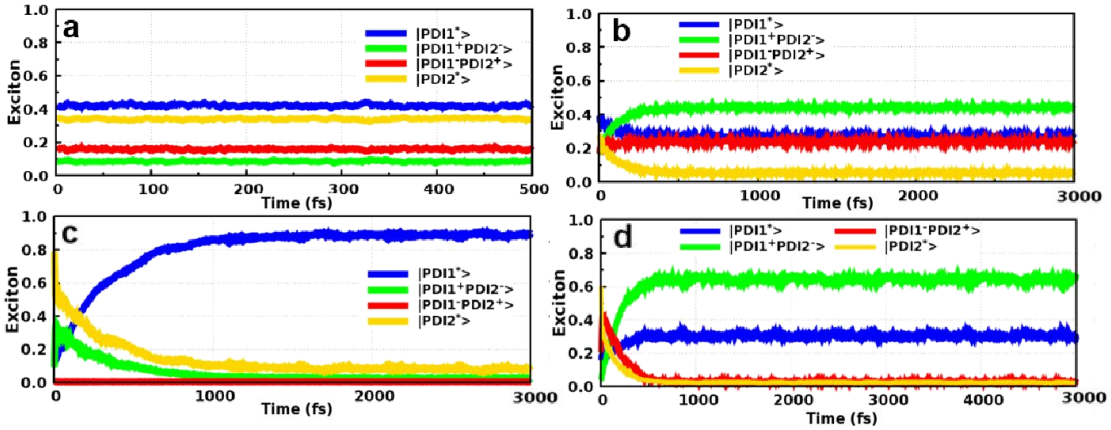

Figure 10. Time-dependent weights of different excitons for PDI-CH_3 in (a) the gas phase and (b) DCM, and for PDI-iso in (c) the gas phase and (d) DCM.

Supporting information

Supporting information can be downloaded here.

References

[1] Deng S., Wang N., Zhu Y. and Thummavichai K., Innovations in nanocomposite photocatalysts for CO_2 to CH3OH conversion. *Catal. Sci. Technol.*, **14** (2024), 6443–6465.

[2] Liu X., Xiao J., Ma S., Shi C., Pan L. and Zou J.J., Review on bismuth-based photocatalyst for CO_2 conversion. *ChemNanoMat*, **7** (2021), 684–698.

[3] Freitas J., Coelho P.J. and Ferreira A.F., Computational investigation of the effect of geometry and fuel composition on the performance of a solid oxide fuel cell. *J. Phys.: Conf. Ser.*, **2766** (2024), 012105.

[4] Qi Y., Lu J. and Liu T., Measuring energy transition away from fossil fuels: a new index. *Renew. Sustain. Energy Rev.*, **200** (2024), 114546.

[5] Ge T.S., Wang R.Z., Xu Z.Y., Pan Q.W., Du S., Chen X.M., Ma T., Wu X.N., Sun X.L. and Chen J.F., Solar heating and cooling: present and future development. *Renew. Energy*, **126** (2018), 1126–1140.

[6] Kumar T., Kumar M., Kumar A., Kumar R. and Bag M., A review of current progress in perovskite-based energy storage to photorechargeable systems. *Energy Fuels*, **39** (2025), 9185–9231.

[7] Sansaniwal S.K., Sharma V. and Mathur J., Energy and exergy analyses of various typical solar energy applications: a comprehensive review. *Renew. Sustain. Energy Rev.*, **82** (2018), 1576–1601.

[8] Borode A., Tshephe T. and Olubambi P., A critical review of the thermophysical properties and applications of carbon-based hybrid nanofluids in solar thermal systems. *Front. Energy Res.*, **12** (2025).

[9] Malhotra S.S., Ahmed M., Gupta M.K. and Ansari A., Metal-free and natural dye-sensitized solar cells: recent advancements and future perspectives. *Sustain. Energy Fuels*, **8** (2024), 4127–4163.

[10] Chen B., Yang Z., Jia Q., Ball R.J., Zhu Y. and Xia Y., Emerging applications of metal-organic frameworks and derivatives in solar cells: recent advances and challenges. *Mater. Sci. Eng. R Rep.*, **152** (2023), 100714.

[11] Sasikumar R., Thirumalaisamy S., Kim B. and Hwang B., Dye-sensitized solar cells: insights and research divergence towards alternatives. *Renew. Sustain. Energy Rev.*, **199** (2024), 114549.

[12] Tamrakar E., Singla R., Patel R.N., Kumar A., Tamrakar R.K. and Butolia S., Review on energy storage applications using new developments in solar photovoltaic materials and systems. *Chem. Pap.*, **79** (2025), 21–42.

[13] Madhu M., Ramakrishnan R., Vijay V. and Hariharan M., Free charge carriers in homo-sorted π-stacks of donor–acceptor conjugates. *Chem. Rev.*, **121** (2021), 8234–8284.

[14] Xiang T.F., Liu Z., Zheng T., Yang L., Tamiaki H., Sasaki S.I., Li A. and Wang X.F., Coherent charge transfer reveals a different theoretical limit of power conversion efficiency in organic solar cells. *J. Phys. Chem. Lett.*, **15** (2024), 9335–9341.

[15] Wang Z., Guo Y., Liu X., Shu W., Han G., Ding K., Mukherjee S., Zhang N., Yip H.L., Yi Y., Ade H. and Chow P.C.Y., The role of interfacial donor–acceptor percolation in efficient and stable all-polymer solar cells. *Nat. Commun.*, **15** (2024), 1212.

[16] Yao L., Liu S., Li L., Ge B., Jiao W., Zong S., Song X., Zhou D. and Liang Z., Enhancing the efficiency and durability of perovskite solar cells by donor–acceptor covalent organic framework with thiazolo[5,4-d]thiazole unit. *CCS Chem.*, **6** (2023), 1721–1730.

[17] Tong Y., Xiao Z., Du X., Zuo C., Li Y., Lv M., Yuan Y., Yi C., Hao F., Hua Y., Lei T., Lin Q., Sun K., Zhao D., Duan C.,

Shao X., Li W., Yip H.L., Xiao Z., Zhang B., Bian Q., Cheng Y., Liu S., Cheng M., Jin Z., Yang S. and Ding L., Progress of the key materials for organic solar cells. *Sci. China Chem.*, **63** (2020), 758–765.

[18] Antolin E., Urieta-Mora J., Molina-Ontoria A. and Martín N., Organic solar cells: principles, materials, and working mechanism. *Curr. Opin. Colloid Interface Sci.*, **76** (2025), 101893.

[19] Ans M., Ayub K., Muhammad S. and Iqbal J., Development of fullerene free acceptors molecules for organic solar cells: a step way forward toward efficient organic solar cells. *Comput. Theor. Chem.*, **1161** (2019), 26–38.

[20] Zhang C., Langner S., Mumyatov A.V., Anokhin D.V., Min J., Perea J.D., Gerasimov K.L., Osvet A., Ivanov D.A., Troshin P., Li N. and Brabec C.J., Understanding the correlation and balance between the miscibility and optoelectronic properties of polymer–fullerene solar cells. *J. Mater. Chem. A*, **5** (2017), 17570–17579.

[21] Mahadevan S., Liu T., Pratik S.M., Li Y., Ho H.Y., Ouyang S., Lu X., Yip H.L., Chow P.C.Y., Brédas J.L., Coropceanu V. and So S.K., Assessing intra- and inter-molecular charge transfer excitations in non-fullerene acceptors using electroabsorption spectroscopy. *Nat. Commun.*, **15** (2024), 2393.

[22] Song Y., Liu X., Li Y., Nguyen H.H., Duan R., Kubarych K.J., Forrest S.R. and Ogilvie J.P., Mechanistic study of charge separation in a nonfullerene organic donor–acceptor blend using multispectral multidimensional spectroscopy. *J. Phys. Chem. Lett.*, **12** (2021), 3410–3416.

[23] Chan W.L. and Rijal K., Entropy-driven charge separation: a potential explanation for the low energy loss found in OPVs with non-fullerene acceptors. *J. Phys. Chem. C*, **128** (2024), 687–696.

[24] Zhang W., Lu H., Li J., Zhan X. and Song Y., The role of the third component in a ternary organic donor–acceptor heterojunction blend based on large-size fused-ring electron acceptors. *J. Phys. Chem. C*, **129** (2025), 11518–11526.

[25] Gao J., Shao J., Li H., Li N., Chen D., Xu Q. and Lu J., Synergistic effect of carbon-deficient and Rh2O3-decorated on carbon nitride: robust photocatalyst for bisphenol a degradation and the mechanism insight. *Sep. Purif. Technol.*, **325** (2023), 124670.

[26] Li X., Xu J., Li L., Zhao S., Mao M., Liu Z. and Li Y., Construction of amorphous CoS/CdS nanoparticles heterojunctions for visible–light–driven photocatalytic H2 evolution. *Catal. Lett.*, **151** (2021), 2408–2419.

[27] Jiang Y.Y., Liu F. and Zhu X.Z., Single-junction organic solar cells with a power conversion efficiency of more than 20%. *Nat. Energy*, **9** (2024), 930–931.

[28] Ding R., Zhang X. and Sun X.W., Organometal trihalide perovskites with intriguing ferroelectric and piezoelectric properties. *Adv. Funct. Mater.*, **27** (2017), 1702207.

[29] Li C. and Wonneberger H., Perylene imides for organic photovoltaics: yesterday, today, and tomorrow. *Adv. Mater.*, **24** (2012), 613–636.

[30] Rajaram S., Shivanna R., Kandappa S.K. and Narayan K.S., Nonplanar perylene diimides as potential alternatives to fullerenes in organic solar cells. *J. Phys. Chem. Lett.*, **3** (2012), 2405–2408.

[31] Zhang G., Zhao J., Chow P.C.Y., Jiang K., Zhang J., Zhu Z., Zhang J., Huang F. and Yan H., Nonfullerene acceptor molecules for bulk heterojunction organic solar cells. *Chem. Rev.*, **118** (2018), 3447–3507.

[32] Cheng P., Li G., Zhan X. and Yang Y., Next-generation organic photovoltaics based on non-fullerene acceptors. *Nat. Photonics*, **12** (2018), 131–142.

[33] Lin Y., Wang Y., Wang J., Hou J., Li Y., Zhu D. and Zhan X., A star-shaped perylene diimide electron acceptor for high-performance organic solar cells. *Adv. Mater.*, **26** (2014), 5137–5142.

[34] Zhong Y., Trinh M.T., Chen R., Wang W., Khlyabich P.P., Kumar B., Xu Q., Nam C.Y., Sfeir M.Y., Black C., Steigerwald M.L., Loo Y.L., Xiao S., Ng F., Zhu X.Y. and Nuckolls C., Efficient organic solar cells with helical perylene diimide electron acceptors. *J. Am. Chem. Soc.*, **136** (2014), 15215–15221.

[35] Meng D., Sun D., Zhong C., Liu T., Fan B., Huo L., Li Y., Jiang W., Choi H., Kim T., Kim J.Y., Sun Y., Wang Z. and Heeger A.J., High-performance solution-processed non-fullerene organic solar cells based on selenophene-containing perylene bisimide acceptor. *J. Am. Chem. Soc.*, **138** (2016), 375–380.

[36] Wu Q., Zhao D., Schneider A.M., Chen W. and Yu L., Covalently bound clusters of alpha-substituted PDI-rival electron acceptors to fullerene for organic solar cells. *J. Am. Chem. Soc.*, **138** (2016), 7248–7251.

[37] Wang H., Chen L. and Xiao Y., A simple molecular structure of ortho-derived perylene diimide diploid for non-fullerene organic solar cells with efficiency over 8%. *J. Mater. Chem. A*, **5** (2017), 22288–22296.

[38] Zhang J., Li Y., Huang J., Hu H., Zhang G., Ma T., Chow P.C.Y., Ade H., Pan D. and Yan H., Ring-fusion of perylene diimide acceptor enabling efficient nonfullerene organic solar cells with a small voltage loss. *J. Am. Chem. Soc.*, **139** (2017), 16092–16095.

[39] Zhang G.J., Feng J.R., Xu X.P., Ma W., Li Y. and Peng Q., Perylene diimide-based nonfullerene polymer solar cells with over 11% efficiency fabricated by smart molecular design and supramolecular morphology optimization. *Adv. Funct. Mater.*, **29** (2019), 1906587.

[40] Liu Y., Mu C., Jiang K., Zhao J., Li Y., Zhang L., Li Z., Lai J.Y.L., Hu H., Ma T., Hu R., Yu D., Huang X., Tang B.Z. and Yan H., A tetraphenylethylene core-based 3D structure small molecular acceptor enabling efficient non-fullerene organic solar cells. *Adv. Mater.*, **27** (2015), 1015–1020.

[41] Liu S.Y., Wu C.H., Li C.Z., Liu S.Q., Wei K.H., Chen H.Z. and Jen A.K.Y., A tetraperylene diimides based 3D nonfullerene acceptor for efficient organic photovoltaics. *Adv. Sci.*, **2** (2015), 1500014.

[42] Wang H., Li M., Liu Y., Song J., Li C. and Bo Z., Perylene diimide based star-shaped small molecular acceptors for high efficiency organic solar cells. *J. Mater. Chem. C*, **7** (2019), 819–825.

[43] Wu M., Yi J.P., Chen L., He G., Chen F., Sfeir M.Y. and Xia J., Novel star-shaped helical perylene diimide electron acceptors for efficient additive-free nonfullerene organic solar cells. *ACS Appl. Mater. Interfaces*, **10** (2018), 27894–27901.

[44] Kong J., Zhang W., Li G., Huo D., Guo Y., Niu X., Wan Y., Tang B. and Xia A., Excited-state symmetry-breaking charge separation dynamics in multibranched perylene diimide molecules. *J. Phys. Chem. Lett.*, **11** (2020), 10329–10339.

[45] Alzola J.M., Tcyrulnikov N.A., Brown P.J., Marks T.J., Wasielewski M.R. and Young R.M., Symmetry-breaking charge separation in phenylene-bridged perylenediimide dimers. *J. Phys. Chem. A*, **125** (2021), 7633–7643.

[46] Mazumder A., Vinod K., Maret P.D., Das P.P. and Hariharan M., Symmetry-breaking charge separation mediated triplet population in a perylenediimide trimer at the single-molecule level. *J. Phys. Chem. Lett.*, **15** (2024), 5896–5904.

[47] Segalina A., Assfeld X., Monari A. and Pastore M., Computational modeling of exciton localization in self-assembled perylene helices: effects of thermal motion and aggregate size. *J. Phys. Chem. C*, **123** (2019), 6427–6437.

[48] Dixit S.J.N., Chacko S., Manna B. and Agarwal N., Ultrafast dynamics of photoinduced electron transfer in bay-aryl-substituted perylene diimide derivatives. *J. Phys. Chem. B*, **126** (2022), 5908–5919.

[49] Polkehn M., Tamura H., Eisenbrandt P., Haacke S., Mery S. and Burghardt I., Molecular packing determines charge separation in a liquid crystalline bisthiophene-perylene diimide donor-acceptor material. *J. Phys. Chem. Lett.*, **7** (2016), 1327–1334.

[50] Xu D.H., Chen Y., Zhang S.Y., Yu J.L., Liu X.Y. and Li L.C., Excitation wavelength-dependent charge generation dynamics in a nonfullerene organic solar cell interface. *Sol. RRL*, **5** (2021), 2000719.

[51] Liu S., Liu S.S., Tang X.M., Liu X.Y., Yang J.J., Cui G.L. and Li L., Solvent effects on the photoinduced charge separation dynamics of directly linked zinc phthalocyanine-perylenediimide dyads: a nonadiabatic dynamics simulation with an optimally tuned screened range-separated hybrid functional. *Phys. Chem. Chem. Phys.*, **25** (2023), 28452–28464.

[52] Zhang S., Zeng Y.P., Wan X.J., Xu D.H., Liu X.Y., Cui G.L. and Li L., Ultrafast exciton delocalization and localization dynamics of a perylene bisimide quadruple π-stack: a nonadiabatic dynamics simulation. *Phys. Chem. Chem. Phys.*, **24** (2022), 7293–7302.

[53] Fang S., Zhou J., Zhou X., Wang C., Jiang N., Liu L. and Xie Z., Interchromophore rotation-related ultrafast charge separation at excited states in head-to-tail linked perylene diimide dyads. *J. Phys. Chem. C*, **123** (2019), 23306–23311.

[54] Li G.Y., Wei X., Zhong H., Liu X.Y., Zhang S., Li L. and Yang J.J., Symmetry breaking and solvent effects regulated photoinduced dynamics in the PDI dimer linked via the imide N-position: a nonadiabatic dynamics simulation. *J. Phys. Chem. A*, **129** (2025), 6211–6225.

[55] Mao D., Chen X.R., Li D.H., Liu X.Y., Cui G.L. and Li L., Ultrafast charge transfer in a nonfullerene all-small-molecule organic solar cell: a nonadiabatic dynamics simulation with optimally tuned range-separated functional. *Phys. Chem. Chem. Phys.*, **24** (2022), 27173–27183.

[56] Ditchfield R., Hehre W.J. and Pople J.A., Self-consistent molecular-orbital methods, IX, an extended Gaussian-type basis for molecular-orbital studies of organic molecules. *J. Chem. Phys.*, **54** (1971), 724–728.

[57] Grimme S., Antony J., Ehrlich S. and Krieg H., A consistent and accurate ab initio parametrization of density functional dispersion correction (DFT-D) for the 94 elements H-Pu. *J. Chem. Phys.*, **132** (2010), 154104.

[58] Hariharan P.C. and Pople J.A., The influence of polarization functions on molecular orbital hydrogenation energies. *Theor. Chim. Acta*, **28** (1973), 213–222.

[59] Parr R.G. and Yang W.T., Density-Functional Theory of Atoms and Molecules. Oxford University Press, New York, 1994.

[60] Perdew J.P., Burke K. and Ernzerhof M., Generalized gradient approximation made simple. *Phys. Rev. Lett.*, **77** (1996), 3865–3868.

[61] Zheng Z., Egger D.A., Brédas J.L., Kronik L. and Coropceanu V., Effect of solid-state polarization on charge-transfer excitations and transport levels at organic interfaces from a screened range-separated hybrid functional. *J. Phys. Chem. Lett.*, **8** (2017), 3277–3283.

[62] Liu S., Liu S.S., Tang X.M., Liu X.Y., Yang J.J., Cui G.L. and Li L., Solvent effects on the photoinduced charge separation dynamics of directly linked zinc phthalocyanine-perylenediimide dyads: a nonadiabatic dynamics simulation with an optimally tuned screened range-separated hybrid functional. *Phys. Chem. Chem. Phys.*, **25** (2023), 28452–28464.

[63] Liu S.S., Wei X., Zheng Y., Liu S., Xu D.H., Li L., Cui G.L. and Liu X.Y., Conformational and solvent effects on the photoinduced electron transfer dynamics of a zinc phthalocyanine-benzoperylenetriimide conjugate: a nonadiabatic dynamics simulation. *ChemPhysChem*, **26** (2025), e202400631.

[64] Sun H. and Autschbach J., Electronic energy gaps for π-conjugated oligomers and polymers calculated with density functional theory. *J. Chem. Theory Comput.*, **10** (2014), 1035–1047.

[65] Cui G.L. and Thiel W., Generalized trajectory surface-hopping method for internal conversion and intersystem crossing. *J. Chem. Phys.*, **141** (2014), 124101.

[66] Liu X.Y., Xie X.Y., Fang W.H. and Cui G.L., Photoinduced relaxation dynamics of nitrogen-capped silicon nanoclusters: a TD-DFT study. *Mol. Phys.*, **116** (2018), 869–884.

[67] Liu X.Y., Li Z.W., Fang W.H. and Cui G.L., Nonadiabatic dynamics simulations on internal conversion and intersystem crossing processes in gold(I) compounds. *J. Chem. Phys.*, **149** (2018), 044301.

[68] Liu X.Y., Zhang Y.H., Fang W.H. and Cui G.L., Early-time excited-state relaxation dynamics of iridium compounds: distinct roles of electron and hole transfer. *J. Phys. Chem. A*, **122** (2018), 5518–5532.

[69] Ryabinkin I.G., Nagesh J. and Izmaylov A.F., Fast numerical evaluation of time-derivative nonadiabatic couplings for mixed quantum–classical methods. *J. Phys. Chem. Lett.*, **6** (2015), 4200–4203.

[70] Granucci G., Persico M. and Zoccante A., Including quantum decoherence in surface hopping. *J. Chem. Phys.*, **133** (2010), 134111.

[71] Hammes-Schiffer S. and Tully J.C., Proton transfer in solution: molecular dynamics with quantum transitions. *J. Chem. Phys.*, **101** (1994), 4657–4667.

[72] Tully J.C. and Preston R.K., Trajectory surface hopping approach to nonadiabatic molecular collisions: the reaction of H^+ with D_2. *J. Chem. Phys.*, **55** (1971), 562–572.

[73] Akimov A.V., Neukirch A.J. and Prezhdo O.V., Theoretical insights into photoinduced charge transfer and catalysis at oxide interfaces. *Chem. Rev.*, **113** (2013), 4496–4565.

[74] Akimov A.V. and Prezhdo O.V., The PYXAID program for non-adiabatic molecular dynamics in condensed matter systems. *J. Chem. Theory Comput.*, **9** (2013), 4959–4972.

[75] Akimov A.V. and Prezhdo O.V., Nonadiabatic dynamics of charge transfer and singlet fission at the pentacene/C_{60} interface. *J. Am. Chem. Soc.*, **136** (2014), 1599–1608.

[76] Hoover W.G., Canonical dynamics: equilibrium phase-space distributions. *Phys. Rev. A*, **31** (1985), 1695–1697.

[77] Nosé S., A unified formulation of the constant temperature molecular dynamics methods. *J. Chem. Phys.*, **81** (1984), 511–519.

[78] Li L., Long R., Bertolini T. and Prezhdo O.V., Sulfur adatom and vacancy accelerate charge recombination in MoS_2 but by different mechanisms: time-domain ab initio analysis. *Nano Lett.*, **17** (12) (2017), 7962–7967.

[79] Zhang Z., Fang W.H., Tokina M.V., Long R. and Prezhdo O.V., Correction for rapid decoherence suppresses charge recombination in multilayer 2D halide perovskites: time-domain ab initio analysis. *Nano Lett.*, **18** (5) (2018), 3312.

[80] Liu X.Y., Chen W.K., Fang W.H. and Cui G.L., Nonadiabatic dynamics simulations for photoinduced processes in molecules and semiconductors: methodologies and applications. *J. Chem. Theory Comput.*, **19** (23) (2023), 8491–8522.

[81] Liu X.Y., Li Z.W., Fang W.H. and Cui G.L., Nonadiabatic exciton and charge separation dynamics at interfaces of zinc phthalocyanine and fullerene: orientation does matter. *J. Phys. Chem. A*, **124** (37) (2020), 7388–7398.

[82] Frisch M.J., Trucks G.W., Schlegel H.B., Scuseria G.E., Robb M.A., Cheeseman J.R., Scalmani G., Barone V., Mennucci B., Petersson G.A., Nakatsuji H., et al., Gaussian 09, Revision D01. Gaussian, Inc., Wallingford, CT, 2009.

[83] Lu T., optDFTw Program v1.0, 2016.

[84] Goedecker S., Teter M. and Hutter J., Separable dual-space Gaussian pseudopotentials. *Phys. Rev. B*, **54** (1996), 1703–1710.

[85] Hartwigsen C., Goedecker S. and Hutter J., Relativistic separable dual-space Gaussian pseudopotentials from H to Rn. *Phys. Rev. B*, **58** (1998), 3641–3662.

[86] Krack M., Pseudopotentials for H to Kr optimized for gradient-corrected exchange-correlation functionals. *Theor. Chem. Acc.*, **114** (2005), 145–152.

[87] Kühne T.D., Iannuzzi M., Del Ben M., Rybkin V.V., Seewald P., Stein F., Laino T., Khaliullin R.Z., Schütt O., Schiffmann F., Golze D., Wilhelm J., Chulkov S., Bani-Hashemian M.H., Weber V., Borštnik U., Taillefumier M., Jakobovits A.S., Lazzaro A., Pabst H., Müller T., Schade R., Guidon M., Andermatt S., Holmberg N., Schenter G.K., Hehn A., Bussy A., Belleflamme F., Tabacchi G., Glöß A., Lass M., Bethune I., Mundy C.J., Plessl C., Watkins M., VandeVondele J., Krack M. and Hutter J., CP2K: an electronic structure and molecular dynamics software package – Quickstep: efficient and accurate electronic structure calculations. *J. Chem. Phys.*, **152** (2020), 194103.

[88] VandeVondele J. and Hutter J., Gaussian basis sets for accurate calculations on molecular systems in gas and condensed phases. *J. Chem. Phys.*, **127** (2007), 114105.

[89] VandeVondele J., Krack M., Mohamed F., Parrinello M., Chassaing T. and Hutter J., Quickstep: fast and accurate density functional calculations using a mixed Gaussian and plane waves approach. *Comput. Phys. Commun.*, **167** (2005), 103–128.

[90] Liu Z., Lu T. and Chen Q., An sp-hybridized all-carboatomic ring, cyclo[18]carbon: electronic structure, electronic spectrum, and optical nonlinearity. *Carbon*, **165** (2020), 461–467.

[91] Lu T. and Chen F., Multiwfn: a multifunctional wavefunction analyzer. *J. Comput. Chem.*, **33** (2012), 580–592.

[92] Barbatti M., Aquino A.J.A. and Lischka H., The UV absorption of nucleobases: semi-classical ab initio spectra simulations. *Phys. Chem. Chem. Phys.*, **12** (2010), 4959–4967.

[93] Crespo-Otero R. and Barbatti M., Spectrum simulation and decomposition with nuclear ensemble: formal derivation and application to benzene, furan and 2-phenylfuran. *Theor. Chem. Acc.*, **131** (2012), 1237.